35th Symposium on Naval Hydrodynamics
Nantes, France, 7 July - 12 July 2024

Large Eddy Simulation of the Tip Leakage Flow in a Ducted Propulsor

T. Leasca[1,2], T. Kroll[3], and K. Mahesh[1]
([1]University of Michigan, USA, [2]Naval Surface Warfare Center, Carderock Division, USA [3]University of Minnesota, USA)

Abstract

Large-Eddy Simulation (LES) is performed to study the tip vortex flow in a ducted propulsor geometry replicating the experiments of Chesnakas and Jessup (2003); Oweis et al. (2006b) and Oweis et al. (2006a). Inception of cavitation in these marine propulsion systems is closely tied to the unsteady interactions between multiple vortices in the tip region. LES is used to shed insight into the structure of the tip vortex flow across a range of operating conditions. Simulation results are able to predict propeller loads within experimental scatter and show agreement with LDV measurements of the mean flow in the blade wake at design advance ratio, $J = 0.98$.

Results show the pressure differential across the blade produces a leakage vortex which separates off the suction side blade tip upstream of the trailing edge. The separation sheet aft of the primary vortex separation point is shown to take the form of a skewed shear layer which produces a complex arrangement of unsteady vortices co- and counter-rotating with the primary vortex. Vortices oriented parallel to the leakage flow are seen to produce instantaneous low-pressure regions wrapping helically around the primary vortex core. Such low pressure regions are seen both upstream and downstream of the propeller blade trailing edge. The trailing edge wake is not found to have any persistent low-pressure vortex core. Statistics of instantaneous low pressures below the minimum mean pressure are found to be concentrated in the region of the blade's trailing edge wake merging with the primary vortex core. The rollup of the leakage flow duct boundary layer behind the trailing edge is also seen to produce counter-rotating vortices which interact with the primary leakage vortex further downstream.

Introduction

Rotating propeller blades are used to produce thrust in marine engineering applications by creating a pressure differential between the upstream and downstream sides of the blade. A tip vortex forms on any finite span blade when the high pressure on the downstream side of the propeller drives flow up and over the blade tip to where the pressure is much lower. Some propeller designs may enclose the rotating blades in a stationary duct or shroud, which allows for increased loading of the propeller. In such ducted propulsor rotors, the pressure differential between the suction and pressure sides of the blade near the tip is increased, which increases thrust and efficiency. As a result, the amount of circulation that must be shed in the blade tip vortices also increases.

Marine propeller design is constrained by cavitation, which is the process by which liquid water transitions to vapor in regions below the vapor pressure. Cavitation can generate unwanted noise, lead to structural vibrations, and cause material erosion. The inception of cavitation is a fundamentally three dimensional and unsteady process, motivating the need for high fidelity modeling. The tip vortex is frequently a location of global minimum pressure, making it a likely place for cavitation inception to occur.

To observe tip vortex cavitation inception in ducted propulsors, two geometrically similar three-bladed propellers P5407 (smaller) and P5206 (larger) were studied in the experiments by Judge et al. (2001); Chesnakas and Jessup (2003); Oweis et al. (2006b) and Oweis et al. (2006a). An important motivation of this experimental campaign was to understand the Reynolds number scaling of tip-vortex inception in ducted propulsors and its difference from open propellers. The flow in the tip vortex region was measured with Laser-Doppler Velocimetry (LDV). Vortex circulation and core radius was reconstructed from the LDV measurements and vortex core pressure was inferred by fitting a Rankine vortex model. The primary tip vortex separates from the blade surface upstream of the trailing edge as a result of the stronger leakage flow in the ducted propulsor. The primary tip vortex also interacts with secondary vortical structures near the blade trailing edge. These flow structures were termed the tip-leakage vortex (TLV) and trailing-edge vortex (TEV). The mutual interaction of these vortices was observed to be related to cavitation inception, which was found to occur further downstream than location of mean low core pressure. It was hypothesized by Chesnakas and Jessup (2003) that inception events occur when the weaker trailing edge vortex is wrapped around the stronger tip leakage vortex before eventually merging further downstream. Small-scale vortical structures undergo strong stretching in this merger process which generates very low pressures. Examination of the instantaneous flow fields in Oweis et al. (2006b) found evidence for this hypothesis, with multiple co-and counter-rotating observed in the LDV measurements behind the trailing edge. Oweis et al. (2006a) studied the smaller P5407 rotor outside the duct configuration, finding that the open rotor has a stronger tip leakage vortex than the ducted rotor.

Propeller P5206 has been studied computationally with Reynolds-Averaged Navier–Stokes (RANS) by Brewer (2002); Kim et al. (2006); Hsiao and Chahine (2006) and Hsiao and Chahine (2008). It was found that the mean low-pressure location predicted is close to the blade tip at 10% of the chord length downstream, similar to the experiments. It was concluded that it is imperative to properly model the unsteady vortex interactions and the resulting low pressure fluctuations.

The fluid dynamics of ducted propulsors are also closely related to those of axial fans and waterjet pumps. Such turbomachinery flows have been studied experimentally by Wu et al. (2011, 2012) and Miorini et al. (2012). They note that turbulence around the leakage vortex is highly anisotropic with various sources and regions of production. Of particular importance is the observation that the jetting shear layer from the suction side blade tip produces new vortex filaments, and transports them to the primary leakage vortex core. These filaments were observed to spiral around the primary TLV before getting entrained.

In the present work, LES is used to study the flow around P5407 at multiple advance ratios. The objectives of this study are to (i) assess and illustrate the ability of LES using an unstructured overset method to predict flow over a ducted propeller in the forward mode of operation, (ii) provide insight into the tip-region associated vortex interactions, (iii) assess the impact of advance ratio on the tip vortex structure, and (iv) examine how the presence of the duct influences circulation shedding.

The paper is organized as follows. The section (titled) “Approach” details the numerical method, geometry discretization, and simulation boundary conditions. The “Validation” section compares simulation results with integrated loads and LDV flow field measurements at the blade trailing edge for both ducted and open rotor configurations. The “Effect of Duct and Advance Ratio” section examines the LES results for a range of advance ratios and discusses how the flow field changes in the absence of the duct. Section “Instantaneous Flow Field” provides a more in-depth discussion of the instantaneous LES results on a finer mesh at the design advance ratio. Additional complexity in the flow field not observed by Chesnakas and Jessup (2003) and Oweis et al. (2006b) is revealed and statistics of intermittent low-pressure events likely to lead to cavitation inception are presented. Finally, the “Mean Flow Field” section uses the time-average LES to investigate the flow features which drive the production of small scale vortices observed in the “Instantaneous Flow Field” section. New instability mechanisms in ducted propulsor tip flows not discussed in previous literature are identified and their importance is revealed by analysis of the Reynolds shear stresses.

Approach

Numerical Method

Large Eddy Simulation (LES) is performed using an unstructured overset method. LES resolves a wide range of turbulent length and time scales to capture the transient behavior of tip vortex interactions. The use of overset grids provides additional flexibility in the grid generation process by allowing meshes to overlap and move in relation to each other. This flexibility also allows for increased resolution with nearly orthogonal hexahedral control volumes in relevant areas near the propeller blades, duct, and tunnel walls while coarsening away from the blade. The incompressible Navier-Stokes equations are solved in an Arbitrary Lagrangian-Eulerian (ALE) formulation where the grid velocity is included in the convection term to avoid tracking multiple reference frames.

The filtered Navier-Stokes equations with the ALE formulation are as follows:

$$\frac{\partial \overline{u}_i}{\partial t} + \frac{\partial}{\partial x_j}(\overline{u}_i\overline{u}_j - \overline{u}_i V_j) = -\frac{\partial \overline{p}}{\partial x_i} + \nu \frac{\partial^2 \overline{u}_i}{\partial x_j \partial x_j} - \frac{\partial \tau_{ij}}{\partial x_j},$$

$$\frac{\partial \overline{u}_i}{\partial x_i} = 0, \tag{1}$$

where u_i is the velocity in the inertial frame, p is the pressure, ν is the kinematic viscosity, V_j is the grid velocity, the overbar $\overline{(\cdot)}$ denotes the spatial filter and $\tau_{ij} = \overline{u_i u_j} - \overline{u}_i\overline{u}_j$ is the sub-grid stress tensor. The sub-grid stress is modeled using the dynamic Smagorinsky model

$$\tau_{ij} = \nu_{SGS}\left(\frac{\partial \overline{u}_i}{\partial x_j} + \frac{\partial \overline{u}_j}{\partial x_i}\right) = \nu_{SGS}\overline{S_{ij}} \tag{2}$$

$$\nu_{SGS} = C_s^2 \Delta^2 |\overline{S_{ij}}| \tag{3}$$

proposed by Germano et al. (1991) and modified by Lilly (1992), where ν_{SGS} is the eddy viscosity, Δ is the grid filter width and C_s is dynamically computed from the solution itself. The Lagrangian time scale is dynamically computed based on a surrogate–correlation of the Germano–identity error (Park and Mahesh, 2009). This approach has shown good performance for a variety of flows including a marine propeller in crashback (Verma and Mahesh, 2012).

Equation 1 is solved using a finite volume segregated predictor-corrector scheme developed in Mahesh et al. (2004). Cartesian velocities and pressure are stored at cell centroids while face-normal velocities are stored separately for face centroids. The grid velocity V_j is assumed to be linear between timesteps and reconstructed from the difference in centroid locations between the current and previous timestep. Cartesian pressure gradients at the centroids are computed using a least-squares formulation. Face values and face-normal gradients required for the finite volume flux evaluations are computed using a nodal reconstruction where the node values are obtained by least-squares from the surrounding cell centroid values. Linear basis functions are then used to integrate the nodal values across the face, as detailed by Horne and Mahesh (2021). At overset grid boundaries, values are interpolated from overlapping meshes using a supercell such that the volume integral of interpolated quantities are conserved (Horne and Mahesh, 2019a)(Horne and Mahesh, 2019b).

Geometry and Discretization

The Propeller 5407 blade and duct geometry is shown in Figure 1. The duct has a uniform cross-section from the inflow to the rotor hub's aft edge. The coordinate x is the direction along the propeller rotation axis, with $x = 0$ representing the nominal rotor disk, located at the middle of the rotor hub. Positive values of x are taken downstream to be downstream of the rotor plane such that the bulk flow through the duct has a positive sign of axial velocity. The azimuthal coordinate $s = R\theta/c$ is taken to be positive aft of the blade tip trailing edge.

The numerical grid is composed entirely of hexahedral cells. Figure 2 shows an $x-R$ slice through the grid with the background mesh shown in blue and the overset meshes shown in green. The narrow tip gap can be seen for one of the three blades above the shaft Figure 2 shows an $x-R$ slice through the grid with the background mesh shown in blue and the overset meshes shown in green. The narrow tip gap can be seen for one of the three blades above the shaft. The gap distance between the blade tip and duct wall is $\Delta r/D = 7.8 \times 10^{-3}$.

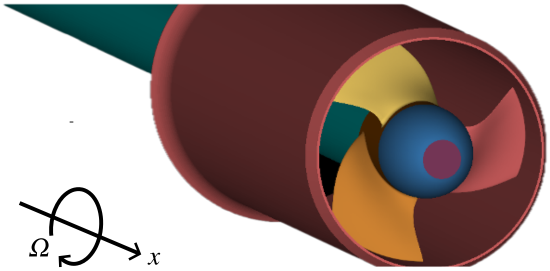

Figure 1: Visualization of the three-bladed propeller P5407 and bellmouth duct. Note that x is the axial direction along the propeller axis. Ω is the direction of propeller rotation here being clockwise around the x axis. Using the right-hand rule, the propeller rotates in the negative θ direction, such that positive $s = R\theta/c$ is behind the blade trailing edge

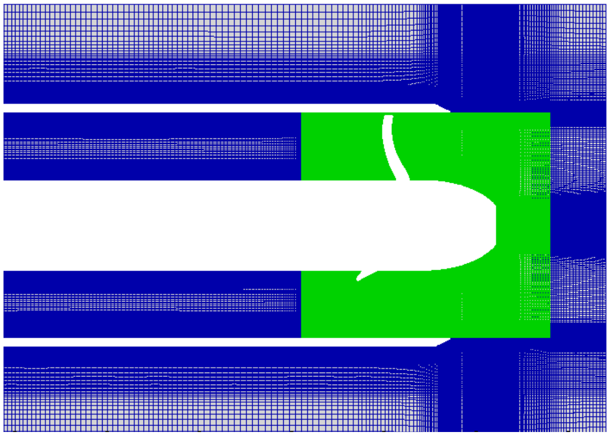

Figure 2: A slice showing the grid for the three-bladed propeller P5407 with a duct. The background grid (blue) and all the overset grids (green). White space represents the negative volume inside the shaft blade and duct solid geometries.

The use of the overset method allows local control of mesh quality and resolution. Figure 3 illustrates the boundaries of the various overset meshes in $x-\theta$ space, with the dashed lines indicating the continuous boundary between $\theta = 0$ and $\theta = 2\pi$ in the azimuthal direction. The most refined mesh is the body-fitted grid copied rotationally for each of the three individual blades of P5407, with boundaries displayed in black. The outer section of the grid in the radial direction is extended $1.0c$ in the downstream θ direction from the propeller blade tip. This is done to maintain the high resolution of the near-blade mesh in the region of the tip vortices trailing behind the blade. The blade grid also resolves the full tip gap between the blade and duct walls without any overset interpolation boundary.

To transition from the high-resolution near-blade mesh to the far field background grid, three layers of intermediate-resolution grids are introduced. Ratios of control volume edge lengths in the overset interpolation fringe are limited to ratios of 3:1 in each direction. The cell edge length aspect ratio in the overset fringe is limited to a maximum of 5. The first transition grid is illustrated in red in Figure 3. It originates just inside the near-blade mesh and surrounds each of the 3 individual blades, and is repeated 3 times. The second transition grid is illustrated in blue and originates just inside the outer boundary of the first transition mesh surrounding each of the three blades. The second transition grid extends around the azimuth. The final transition mesh is displayed in green and provides refinement of the hub boundary layer and wake before transitioning to the background mesh at the outlet of the duct. All grid boundaries are constructed such that no cutting is performed in the solver to remove redundant control volumes. The wall-normal spacings and growth rates are equivalent between all overset meshes to provide accurate interpolation of the turbulent boundary layer flow.

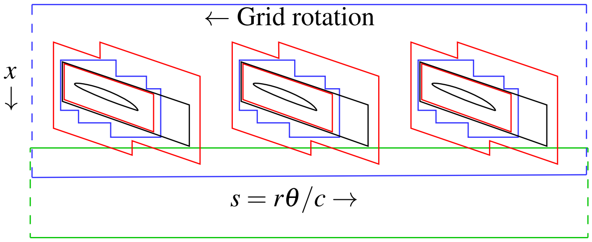

Figure 3: Illustration of the overset grid structure used for P5407 in $x-\theta$ space. Lines denote the boundaries of each overset grid. In order of from finest resolution to coarsest: The black illustrates the near blade, red is the blade shroud, blue is the blade buffer, and green is the hub wake. Dashed lines indicate the boundary around the azimuth between $\theta = 0$ and $\theta = 2\pi$.

Simulation Setup

The inflow into the domain is located $2.1D$ upstream of rotor stack line, which is located at $x = 0$. The computational inflow is just downstream of the bellmouth duct inlet to allow for precise control of the volumetric flow rate to the rotor, as discussed in Chapter 5 of Kroll (2022). The inflow boundary condition is prescribed as a uniform value equal to the mean flow rate through the duct in the experiments of Chesnakas and Jessup (2003) and is equal to $U_{inf,BC} = 0.968U_\infty$. The mean flow rate is found by integrating LDV measurements of the inflow profile taken at $x = -0.3615R$ where R is the propeller radius. The boundary layer is numerically tripped just downstream of the inflow plane at $x = -2D$ by applying a steady wall-normal velocity of 0.06% of U_∞. This numerical tripping results in a fully turbulent inflow to the rotor. A convective boundary condition is set $2D$ downstream of the propeller center in the outlet section. The blades and hub surfaces contained in the rotating grids are given the boundary condition $U_{face} = \Omega \times R$ while the duct surface is given a no-slip boundary condition $U_{face} = 0$. All other surfaces have no-slip boundary conditions. The Reynolds number considered here is

$$Re_{tip} = \frac{\sqrt{U_\infty^2 + (\Omega R)^2}C}{\nu} = 1.1 \times 10^6 \tag{4}$$

Two grid resolutions are considered. The coarse resolution grid achieves each local control volume size in the range $\Delta l^+ = 8-30$ in wall units, while the wall-normal blade and duct resolution in the local normal direction n is $\Delta n^+ = 3.2$. The non-dimensional time step for this case is $\Delta t U_\infty/D = 4 \times 10^{-5}$. An additional case is simulated using a fine, high-resolution grid also at $Re_{tip} = 1.1 \times 10^6$ and a non-dimensional time step of $\Delta t U_\infty/D = 2 \times 10^{-5}$. For the fine grid, the resolutions achieved in the blade grid for each local control volume length l range $\Delta l^+ = 5-18$ in wall units, while the wall-normal blade and duct resolution in the local normal direction n is $\Delta n^+ = 0.96$. All cases are simulated for a total of 10 revolutions or 5 flow domain passes (a flow domain is the length $2D$ of the inner duct). More information on the size and partitioning of the meshes is presented in Tables 1 and 2. More details of the experimental setup and geometry are provided in (Oweis et al., 2006b,a). The simulation is run for enough revolutions for statistical convergence of flow field parameters and loads. Domain flow field statistics and flow field parameter values for regions under vapor pressure that corresponds to $C_p < 5.6$ are collected for additional analysis. These are collected for 4 revolutions or 2 flow domain passes.

Results

Qualitative Description of the Flow

In this section, the global features of the flow are described. Figure 4 (a) shows a photograph of developed vortex cavitation from the experiments of Chesnakas and Jessup (2003). Annotations on the figure detail the description of the key flow features identified by Chesnakas and Jessup (2003) and Oweis et al. (2006b). The photograph is oriented looking down at the blade tip such that the blade rotation causes the tip to move upward in the frame. The bulk flow through the duct moves in the positive x-direction, from left to right. The pressure gradient across the blade results in a leakage flow moving in the negative x-direction in the gap region between the blade and the duct. The leakage flow separates off the

	Background	Blade	Blade Shroud	Blade Buffer	Hub/Wake	Total
Copies	1	3	3	1	1	9
CVs ($\times 10^6$)	47.5	16.4	9.6	38.6	14.4	178
Procs	1696	728	426	1462	640	7260

Table 1: Details for the coarse grid. Copies is the number of grid copies used in the simulation, CVs is the number of control volumes and Procs is the number of processors that the grid is partitioned.

	Background	Blade	Blade Shroud	Blade Buffer	Hub/Wake	Total
Copies	1	3	3	1	1	9
CVs ($\times 10^6$)	96.1	57.3	34.6	131.1	57.0	559.9
Procs	2068	1232	742	2818	1224	12032

Table 2: Details for the fine grid. Grids is the number of grid copies used in the simulation, CVs is the number of control volumes and Procs is the number of processors that the grid is partitioned.

suction side blade tip and rolls up into a coherent vortex, termed the primary leakage vortex hereafter. The primary leakage vortex core is seen to coincide with regions of vapor upstream from the trailing edge. Aft of the trailing edge, an additional region of vapor coincides with the merger of secondary vortex structures from the trailing edge wake. Figure 4 (*b*) shows an isosurface demarcating a low pressure coefficient region of $C_p < -3.9$ from the current LES simulation results colored by vorticity magnitude. The entire low pressure region corresponds to a vorticity magnitude $|\omega| > 200$. The low pressure region follows a qualitatively similar trajectory to the primary leakage vortex observed to cavitate in 4(*a*).

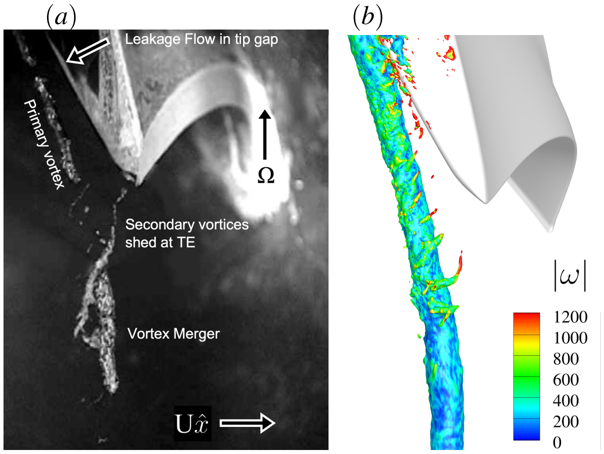

Figure 4: (*a*) Photograph of developed tip vortex cavitation from the experiments of Chesnakas and Jessup (2003) at $\sigma = 5.6$. (*b*) Isosurface of instantaneous $C_p = -3.9$ from the current LES results on the fine grid. The flow field quantities are normalized with U_∞ and R.

Additional qualitative similarities are seen in the orientation and location of secondary vortical structures of higher vorticity magnitude $|\omega| > 600$ merging in the blade wake aft of the trailing edge. An in-depth discussion of the small scale vortex structures near the trailing edge is presented later in section ”Instantaneous Flow Field”.

Validation

In this section, we validate the time-averaged flow statistics and load statistics from the LES simulations against the experiments of Chesnakas and Jessup (2003); Oweis (2003); Oweis et al. (2006b,a). Three-dimensional Laser Doppler Velocimetry (LDV) data is provided by NSWCCD (Thad Michael, personal communication).

The θ direction coordinate is normalized as: $s = R\theta/c$ where R is the propeller radius, θ is the direction of propeller rotation and c is the blade chord. The coordinates are centered at the propeller blade trailing-edge tip where $\theta = 0$ and increases downstream from the blade.

As an assessment of the appropriateness of the mesh resolution, Figure 5 shows a contour of eddy-viscosity ν_{SGS} normalized by the molecular viscosity ν in the tip vortex region at $s = 0$. As seen in Equation 1 and 2, the eddy viscosity is the parameter by which the sub-grid-scale (SGS) model influences the LES solution. The eddy viscosity ratio is therefore a measure of the unresolved turbulent scales and tends to zero as the grid is refined. Figure 5 shows that in the tip vortex interaction region, ν_{SGS}/ν has a maximum of about 6 for the coarse grid and 3 for the fine grid. This suggests sufficient resolution in the vortex interaction areas to minimize the LES subgrid model's influence on the observed flow structure.

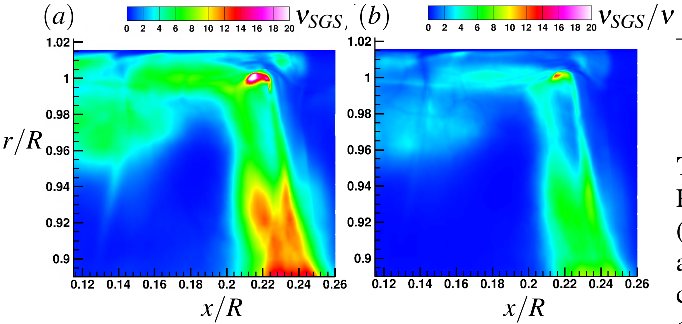

Figure 5: A contour slice in the $x-r$ plane at the propeller trailing-edge tip $s=0$ showing the LES eddy-viscosity ν_{SGS} normalized by the molecular viscosity ν for (*a*) the coarse grid and (*b*) the fine grid. The horizontal axis is x/R and the vertical axis is r/R.

	EXP-1	EXP-2	EXP-3	LES-C	LES-F
Re_{tip}	1.4M	1.4M	1.4M	1.1M	1.1M
$\langle K_T \rangle$	0.278	0.245	0.265	0.273	0.274
$\langle K_Q \rangle$	0.053	0.054	0.054	0.054	0.054

Table 3: Comparison of load statistics for Propeller P5407 at $J = 0.98$ and $Re_{tip} = 1.1 \times 10^6$. EXP-1 is (Chesnakas and Jessup, 2003), EXP-2 is (Oweis, 2003), and EXP-3 is (Oweis et al., 2006a). LES-C is the current simulation on the coarse grid and LES-F is the current simulation fine grid. Data from (Chesnakas and Jessup, 2003) was provided by NSWCCD (Thad Michael, personal communication).

Loads

The time-averaged load statistics from the LES at an advance ratio of $J = 0.98$ are compared to the experiments of Chesnakas and Jessup (2003); Oweis (2003); Oweis et al. (2006b) and Oweis et al. (2006a). The advance ratio is defined as

$$J = \frac{2\pi U_\infty}{\Omega D} \tag{5}$$

where U_∞ is the freestream velocity, Ω is the rotational velocity in units of radians per second, and D is the propeller diameter. The experiments of Chesnakas and Jessup (2003); Oweis et al. (2006b) and Oweis et al. (2006a) adopted the time-average velocity value midway between the hub and duct in the radial direction as U_∞. Note that $U_{inf,BC}$ prescribed at the simulation inflow is chosen such that the volumetric flow rate through the duct reproduced that of the corresponding experiments, as discussed in the preceding section. Table 3 summarizes the mean loads, comparing the LES simulations to various experiments for propeller P5407. The thrust and torque coefficients are defined as

$$K_T = \frac{4\pi^2 T}{\rho \Omega^2 D^4}, K_Q = \frac{4\pi^2 Q}{\rho \Omega^2 D^5} \tag{6}$$

where T is the thrust force, Q is the torque, and ρ is the fluid density. The difference between the LES loads of the coarse and fine grids is 1% for K_T and less than that for K_Q, suggesting grid convergence of the integral circulation. The experimental load data for K_T from three different experiments contains some scatter with a difference of about 13% of K_T. For K_Q, one of the experimental values has a minor 2% difference. For both the coarse and fine resolution grids, the LES shows agreement with the experimental K_Q values and lying with in the scatter for K_T.

Loads are also measured at an advance ratio around $J = 1.1$ for P5407 and compared to the experimental data of Chesnakas and Jessup (provided by Thad Michael, personal communication). It is not clear whether dummy hub corrections for hydrostatic pressure on the dynamometer are already accounted for in this data. Measurements of the inflow were not available, making it difficult to precisely determine the duct mass flow and U_∞ for the calculation of the advance ratio, J. For that reason, a range of inflows velocities, $U_{inf,BC}$ are considered for the same propeller rotation rate corresponding to roughly $J = 1.1$. The data is plotted in Figure 6 and shows that a 1.5% reduction in $U_{inf,BC}$ results in a 13% reduction in the thrust coefficient K_T. Such sensitivity dK_T/dJ matches the experimental results well. The sensitivity is also well predicted for dK_Q/dJ. The data is presented here to highlight the extreme load sensitivity to the inflow of ducted propulsors and to make the case that, for future experiments, integral quantities such as volumetric flow rate are preferred relative to single-point inflow measurements for normalization. This conclusion is especially important when comparisons are being made across different test setups with significantly different Reynolds numbers. Reynolds number variations will modify the boundary layer thicknesses on both the shaft and the duct wall and may therefore result in a different mid-channel velocity for the same mass flow rate. The same effect may also occur when changing propeller rotation rates within the same test setup. Lower rotation rates than the "nominal" condition at which the inflow is measured, such as that considered here, result in a reduction in the favorable pressure gradient experienced by the upstream boundary layer on both the duct and shaft. Weaker favorable pressure gradients result in a thickening of the boundary layer, causing the peak velocity at mid-span to increase assuming the mass flow rate remains constant.

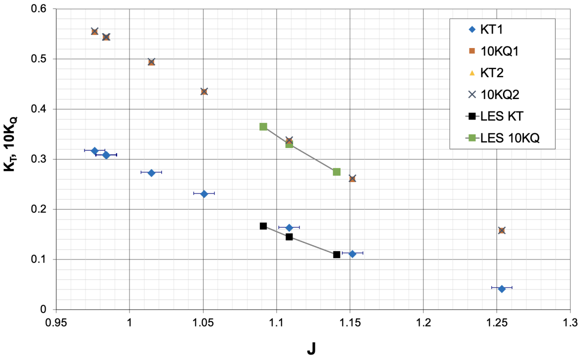

Figure 6: Force coefficients K_T and K_Q across range of J. LES results for the coarse grid are superimposed on data from Chesnakas and Jessup (Personal Communication)

Comparison to Ducted Rotor LDV

The time-averaged flow statistics from the LES are compared to the three-dimensional LDV experimental data of Chesnakas and Jessup (2003). Contour slices are taken at $s = 0$ for each of the three blades in the $x-r$ or axial and radial plane. Chesnakas and Jessup (2003) state that the uncertainty in velocity measurements was 10% of U_∞ at the vortex core location and in the blade wake. The cause of uncertainty was linked to inadequate sample sizes taken in regions of high turbulence. Figure 7 shows the LDV grid on the left compared to the coarse LES numerical grid on the right. The LES solution mesh extends further toward the duct wall than the LDV with points clustered in the duct boundary layer.

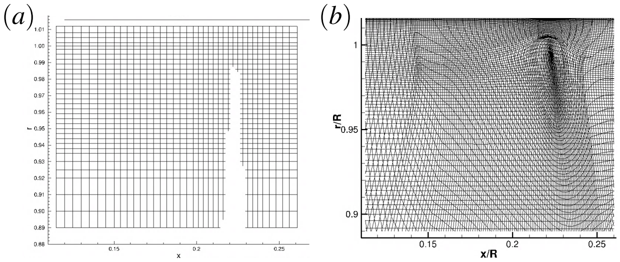

Figure 7: The grid resolutions at the blade trailing edge and in the $x-r$ plane where the horizontal axis is x/R and the vertical axis is r/R. (a) the experiments of Chesnakas and Jessup (2003) and (b) the current LES coarse grid.

Figure 8 compares contour slices of the mean axial velocity U_x at the blade tip in the $x-r$ plane where the axial coordinates are normalized by the propeller radius x/R and r/R. The axial flow is seen to move upstream (negative U_x in blue) above the propeller blade tip radius, which is termed the tip leakage flow. The axial flow maintains a positive sign at values of the radial coordinate below the blade tip. There are discrepancies in the LES and LDV results near the duct surface where the experimental viewing window protrudes into the circular duct cross section and the LDV has a coarser resolution. The LES captures the leakage flow in more detail, including the thin boundary layer on the duct wall.

Figure 9 shows contour slices of the mean θ component of vorticity ω_θ at the blade tip in the $x-r$ plane. The vorticity is mostly directed in the positive θ direction (out of the page or counter-clockwise using the right-hand rule) and peaks at the leakage vortex center. The leakage vortex is formed from the rollup of the leakage flow separating off the blade tip. The leakage vortex is offset from the blade trailing edge in the axial direction. A separation sheet connects the leakage vortex core to the blade tip, visible as a narrow region of high vorticity of the same sign as the leakage vortex core. Wall shear of the reversed leakage flow induces counter-rotating vorticity on the duct wall (opposite ω_θ sign or blue). Upstream of the leakage vortex core, the region of counter-rotating vorticity begins to grow away from the duct wall. The LDV data does not have sufficient resolution to capture the near-wall shear and this does not show the region counter-rotating vorticity.

For a more detailed comparison to the experiment, profiles are taken of both the mean of U_x (Figure 10(a)) and ω_θ (Figure 10(b)) at various locations in the axial direction x/R near the tip leakage vortex core. The mean ω_θ peaks correspond closely and the LES is within the experimental scatter. Differences near the duct wall surface are observed as previously discussed.

A comparison of the locations of the tip leakage vortex center is shown in Table 4. The leakage vortex center is taken to be the location of the maximum mean vorticity. The vortex locations for the three individual blades in the LES mesh are all within 1% of each other, evidence of statistical and grid convergence. For the experiments, some scatter is observed, with differences up to 6% in the axial direction. The LES results agree with the experimental results for Blade 3 within 1.3% for the axial location and 0.6% for the radial location of the vortex center.

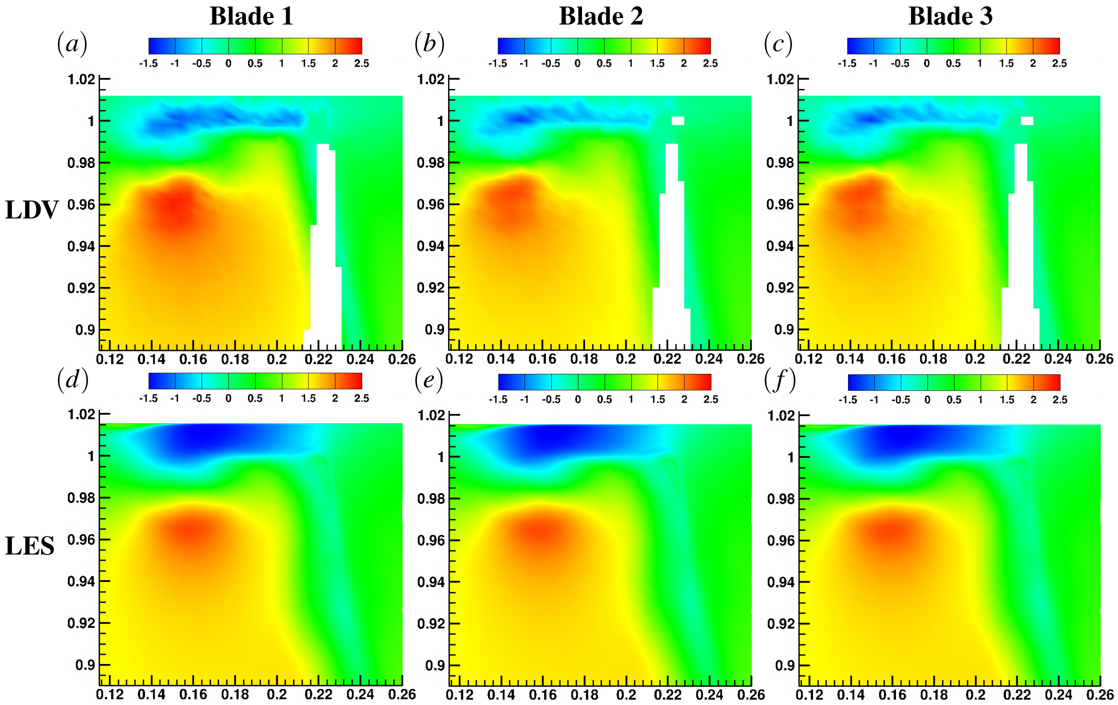

Figure 8: Contours of the mean of the axial velocity U_x for the 3 individual blades at the blade trailing edge and in the $x-r$ plane where the horizontal axis is x/R and the vertical axis is r/R. (a,b,c) are the LDV from the experiments of (Chesnakas and Jessup, 2003). (d,e,f) are the current LES on the coarse grid for the ducted rotor at $J = 0.98$ $Re_{tip} = 1.1 \times 10^6$. The flow field quantities are normalized with U_∞.

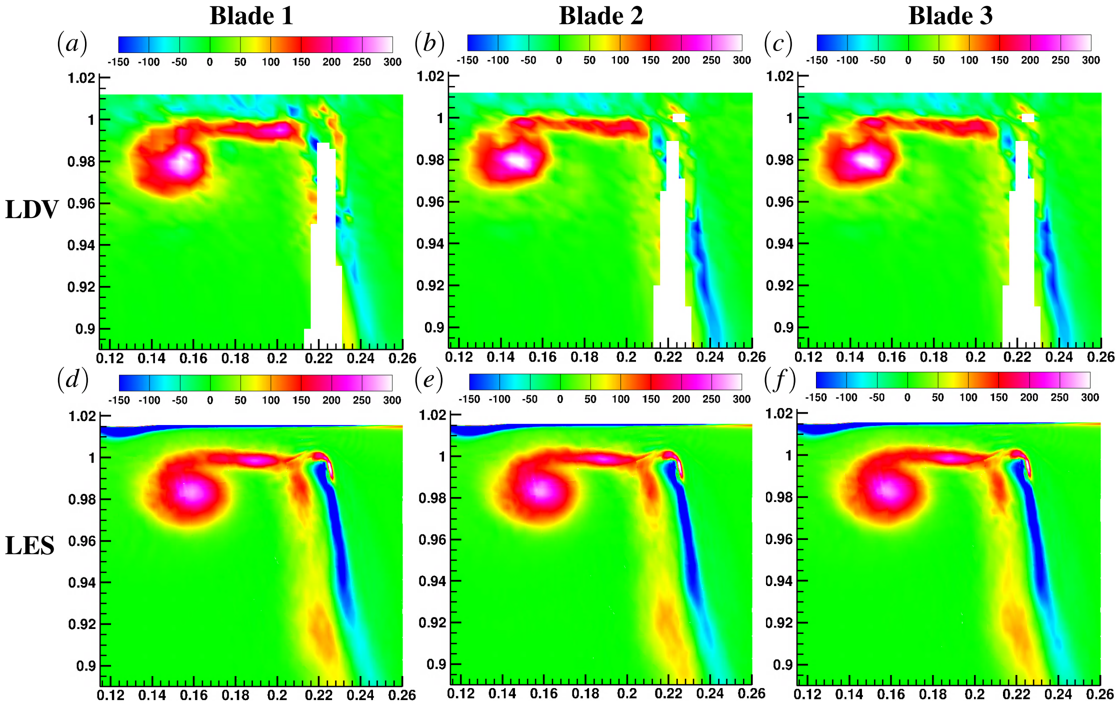

Figure 9: Contours of the mean of the θ component of vorticity ω_θ for the 3 individual blades at the blade trailing edge and in the $x-r$ plane where the horizontal axis is x/R and the vertical axis is r/R. (a,b,c) are the LDV from the experiments of (Chesnakas and Jessup, 2003). (d,e,f) are the current LES on the coarse grid for the ducted rotor at $J = 0.98$ and $Re_{tip} = 1.1 \times 10^6$. The flow field quantities are normalized with U_∞/R.

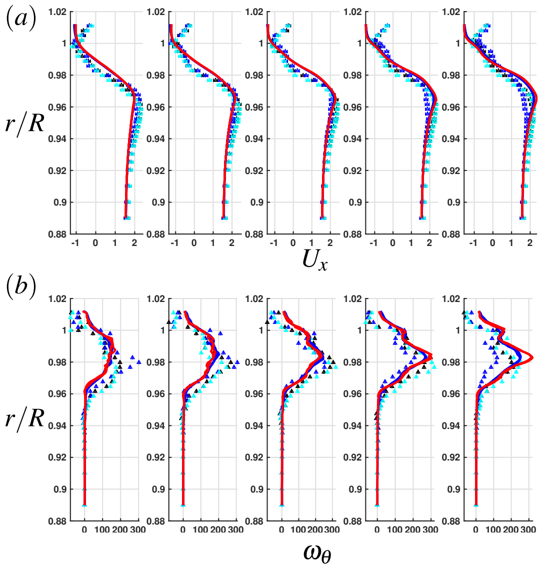

Figure 10: The profiles of the LDV at various axial locations near the TLV center. (a) U_x and (b) ω_θ. The experiments of Chesnakas and Jessup (2003) are the symbols from multiple blades while the LES are the solid lines for the different blades with coarse (blue) and fine (red). The locations are from left to right $x/R = 0.145$, $x/R = 0.150$, $x/R = 0.154$, $x/R = 0.158$, and $x/R = 0.162$. Error bars of the uncertainty from the experiments are only included for U_x. The flow field quantities are normalized appropriately using U_∞ and R.

Comparison to Open Rotor LDV

Comparisons of simulations of P5407 without the duct are also performed on the coarse grid and compared to LDV measurements from Oweis et al. (2006a) in Figure 11. Contour slices are shown for the three velocity components at the blade trailing edge tip in the $x-r$ plane. The coordinates are normalized by the propeller radius x/R and r/R. Figure 11(a) and (b) show the azimuthal velocity component u_θ in the inertial frame. The azimuthal flow is seen to move strongly with the blade in the region immediately behind the trailing edge, corresponding to the region of positive u_θ nearly vertically aligned at $x/R = 0.23$. It can be seen that the underside of the tip vortex is associated with another local maximum of u_θ at $r/R = 0.975$ and $x/R = 0.205$. The location of this local maximum agrees well between the experimental LDV data (a) and LES (b). Figure 11(c) and (d) show the axial velocity component u_x. Above the propeller blade tip radius, $r/R = 1.0$ a reversed tip leakage flow is seen, as in the ducted rotor case. The magnitude and spatial region of the reversed flow above the blade tip agrees well when comparing the experimental LDV measurements (c) and LES (d). Unlike the ducted rotor, the reversed leakage flow is confined to a small region in both the axial and radial directions. It can be seen that, at the same advance ratio, the tip wake flow remains much closer to the blade trailing edge than it does for the ducted rotor. At lower values of the radial coordinate, the axial flow maintains a positive sign. Figures 11(e) and (f) show the radial velocity component. The LDV measurement in (e) displays oscillations near the tip vortex - indicative of inadequate measurement resolution and/or sample size. As with the ducted case, the LDV resolution was coarser than the present coarse LES grid. The radial velocities nevertheless show qualitative agreement between the two, with positive values seen on the pressure side blade wake and negative values on the upstream side of the tip vortex.

Effect of Duct and Advance Ratio

Simulations at 3 different advance ratios, J =1.11, 0.98, and 0.87, are performed using the coarse grid to observe the tip vortex structure across a range of operating conditions. Simulations are also performed of the open rotor without a duct at $J = 0.98$. The open rotor is found to have a similar K_T at $J = 0.98$ as the ducted rotor at $J = 1.11$. This allows for a comparison of the tip vortex's local strength with the same integral circulation around the entire blade.

Figure 12 shows the blade pressure across the range of operating conditions. Figure 12(a) shows the open rotor while Figures 12($b-d$) show the ducted rotor with the advance ratio decreasing from left to right. Strong pressure recovery above ambient pressure is seen at the trailing edge across the blade span for all conditions. The open rotor (a) displays strong low-pressure regions along the aft $1/3^{rd}$ chord of the suction side at the blade tip and at the blade tip leading edge. For the ducted $J = 1.11$ case (b), a similar local region of low pressure is observed at the blade suction side tip near the leading edge. These leading edge tip low pressure regions occur in regions where the axial velocity is positive forcing the flow to accelerate around the blade tip chamfer radius. Notably, the same local low-pressure region is not seen at the $J = 0.98$ ducted case, demonstrating that the presence of the duct modifies the local angle of attack experienced by each blade section.

To examine the blade loading distribution of the various conditions, profiles of negative mean pressure coefficient $-\langle C_p \rangle$ are plotted in Figure 13 for r/R =0.5, 0.6, 0.7, 0.8, 0.9 and 0.98. The horizontal axis is $s = R\theta/c$ and the vertical axis is $-\langle C_p \rangle/100 + r/R$. The azimuthal reference point $\theta = 0$ is taken at the trailing edge of the $r/R = 0.98$ section. Nearer to the blade root, the loading for the $J = 0.98$ ducted and $J = 1.11$ open cases are quite similar. The lower four blade sections show increased suction along the entire mid-chord region for the open

	EXP-1 Blade 1	EXP-1 Blade 2	EXP-1 Blade 3	LES-C Blade 1	LES-C Blade 2	LES-C Blade 3	LES-F Blade 1	LES-F Blade 2	LES-F Blade 3
x/R	0.154	0.148	0.157	0.159	0.158	0.159	0.159	0.158	0.159
r/R	0.979	0.980	0.977	0.983	0.983	0.983	0.983	0.983	0.983

Table 4: Propeller P5407 ($J = 0.98$): The $x - r$ plane mean tip leakage vortex center locations of the experiment of Chesnakas and Jessup (2003) (EXP-1) compared to LES for the coarse $Re_{tip} = 1.1 \times 10^6$ case for the coarse (LES-C) and high resolution (LES-F) grids.

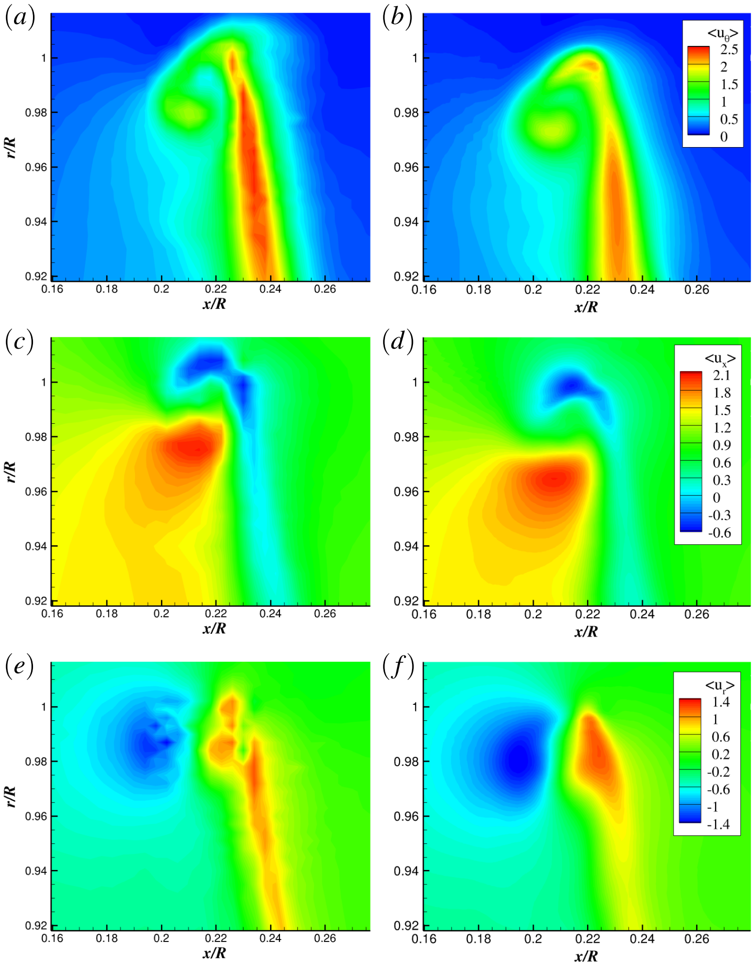

Figure 11: Contours of mean velocity components for the open rotor P5407 comparing LES results and experiments. Contours are shown in the $x - r$ plane at the blade trailing edge where the horizontal axis is x/R and the vertical axis is r/R. (a,c,e) is the LDV from the experiments of (Oweis et al., 2006a). (b,d,f) are the current LES on the coarse grid at $Re_{tip} = 1.1 \times 10^6$. ($a$,$b$) u_θ (c,d) u_x, and (d,e) u_r. The flow field quantities are normalized with U_∞.

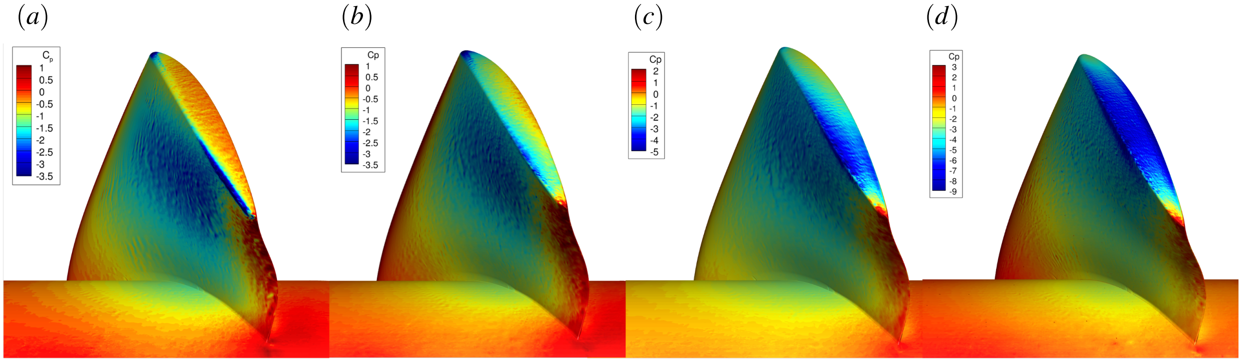

Figure 12: Instantaneous pressure contours on the blade surface across the range of advance ratios (*a*) $J = 0.98$ open, (*b*) $J = 1.11$ ducted, (*c*) $J = 0.98$ ducted, (*d*) $J = 0.87$ ducted. Note that contour levels for (*c*) and (*d*) are changed to allow the spatial variation of pressure across the blade to be visualized at all conditions.

rotor relative to the ducted rotor at the same thrust. At the outermost blade section, the open rotor produces almost no suction near the mid chord, but has a strong suction peak near the trailing edge. Meanwhile, the ducted rotor at the same thrust maintains a similar blade loading shape as the lower sections. Thus, as expected, adding a duct to the same rotor geometry has the effect of increasing the lift generation at the blade tip while decreasing the lift generation near the root when comparing at the same thrust (van Manen, 1962; Kawakita, 1992). Meanwhile, when comparing at the same advance ratio, the ducted rotor has higher suction at all blade sections than the open rotor. Significant differences between the peak suction near the leading edge are also seen for the $J = 0.98$ open and ducted cases for larger values of r/R. This difference in local pressure can be explained by the outer blade sections of the ducted rotor experiencing a different angle of attack than the open rotor case. Meanwhile, the $J = 0.87$ ducted case demonstrates the highest loading at all values of r/R. This larger pressure differential drives a faster leakage flow at the low advance ratio case.

The primary leakage vortex is observed to have significant change in its separation point and trajectory with changing advance ratio. Figure 15 shows isosurfaces of low pressure regions intended to demarcate the primary vortex core. The illustrated threshold of pressure coefficient is therefore altered for the different conditions. In Figure 15(*a*) and (*b*), the illustrated threshold is $C_p = -2.0$ to directly compare the open and ducted rotor at the same thrust. The open rotor is seen to have a lower and more coherent primary vortex than the ducted rotor. The lowest mean pressure coefficient of the tip vortex is $\langle C_p \rangle = -4.3$ for the open rotor and $\langle C_p \rangle = -2.45$ for the ducted rotor at $s = -0.035$ and -0.156, respectively. This finding provides qualitative evidence for the conclusions of Oweis et al. (2006a) that the tip vortex is weaker in ducted propulsors.

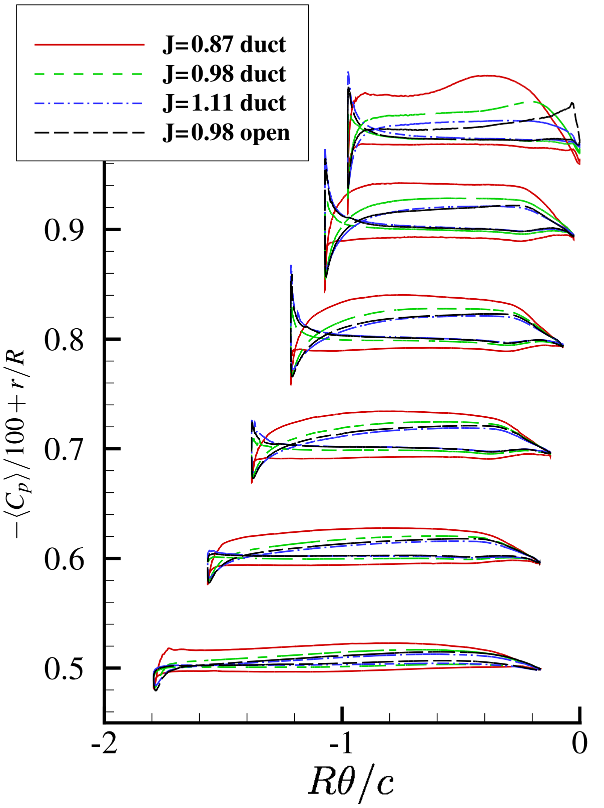

Figure 13: Blade loadings at various radial sections corresponding to $r/R = 0.5, 0.6, 0.7, 0.8, 0.9$ and 0.98. The mean pressure coefficient $\langle C_p \rangle$ is plotted for each section. The azimuthal reference $\theta = 0$ is defined at the trailing edge for $r/R = 0.98$

Figure 15(*a*) and (*b*) also show that the trailing tip vortex follows a different path in $x-\theta$ space, with the open rotor vortex being nearly aligned with the blade tip chord pitch while the ducted tip vortex is aligned more with the azimuthal direction. At the highest advance ratio, shown in (*b*), the pressure on the blade suction side surface is comparable to the vortex core pressure, indicating that sheet/cloud cavitation could occur in addition to or instead of tip vortex cavitation. The leakage vortex separation location is also seen to be sensitive to the tip loading and advance ratio. Even at the same thrust condition of (*a*) and (*b*), the ducted rotor leakage vortex separates upstream from the trailing edge as a result of the increased blade loading forward of the mid-chord, which strengthens the tip leakage flow. The same trend continues as the advance ratio is decreased in Figure 15(*c*) and (*d*), with the leakage vortex of $J=0.87$ (*d*) separating upstream of forward blade suction peak. This has potential significance to the cavitation inception behavior. As discussed in previous sections, additional circulation is fed to the primary vortex via the separation sheet connecting the vortex core to the blade boundary layer, resulting in the vortex strengthening with increasing azimuthal distance s. Thus the region of peak swirl occurs in a region of low ambient pressure away from the blade trailing edge at the lowest advance ratio $J=0.87$. Side lobes of low pressure are seen wrapping helically around the primary vortex core in both 15(*c*) and (*d*). These vortex structures are seen to be aligned with the leakage flow, as is discussed in more detail in later sections examining the fine grid solution at $J=0.98$.

The earlier separation point of the leakage vortex at a lower advance ratio also results in the vortex core having a larger offset distance in the axial direction at the trailing edge. This is further examined in Figure 14, which shows data extracted from the mean flow field immediately aft of the trailing edge at $s=0$. Profiles were extracted in the axial direction at the radial location corresponding to the peak mean vorticity. Radial locations of peak mean vorticity were found to show a small variation between the different configurations with a range of $r/R=0.975$ ($J=0.877$) to $r/R=0.983$ ($J=1.11$). Note that because of the secondary vortices that are also present nearby, the peak of the mean vorticity may not correspond precisely with the peak low pressure. Figure 14(*a*) shows the mean vorticity along the slice on the vertical axis, while the horizontal axis is x/R. The blade tip trailing edge is located at $x/R=0.23$. At this location, all operating conditions show a rapid sign change of the azimuthal vorticity across the blade wake. The pressure side blade wake is strongly negative, while the suction side blade wake is strongly positive. The negative peaks of the curve have been truncated in the figure. The ducted $J=0.87$ mean flow field is seen to contain a single coherent vortex offset from the blade by $\Delta x/R=0.12$ which has the lowest core pressure of any of the configurations. Meanwhile, the ducted $J=1.11$ configuration has the highest primary vortex core pressure and the lowest peak vorticity. For the three ducted cases, the distance between the the primary vortex core and the trailing edge blade wake decreases with increasing advance ratio. At the $J=1.11$ condition, the primary vortex is close enough to the trailing edge such that the vorticity does not drop to zero in the intermediate region between the vortex core and the blade wake. This results in the tail of the low pressure region associated with the primary vortex core having a skew towards the downstream $+x$ direction. The pressure minimum is co-located with the upstream vorticity peak of the primary leakage vortex. The open rotor at $J=0.98$ is seen to have a vorticity peak slightly above that of the ducted $J=0.87$ rotor. This can be explained by the strong pressure gradient across the tip gap forming exclusively in the aft-most part of the blade, as seen in Figure 13. The core pressure of the open rotor tip vortex is higher than the primary vortex at the ducted $J=0.87$ or $J=0.97$ condition.

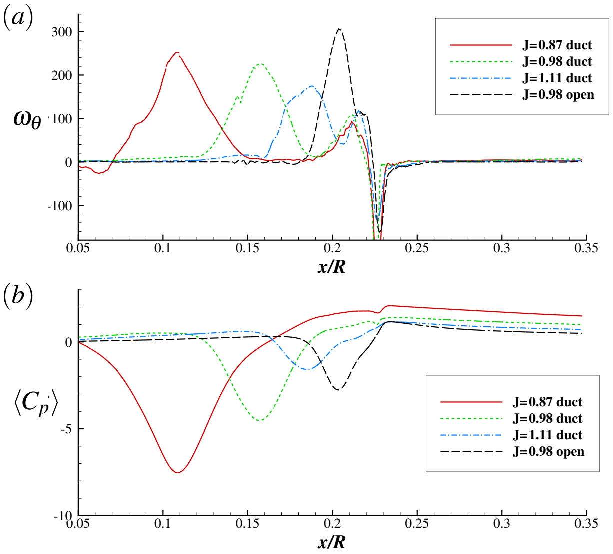

Figure 14: Extracts of the tip flow field at $s=0$ and r/R corresponding to the location of mean azimuthal vorticity $r/R\approx 0.98$. (*a*) shows the mean azimuthal vorticity $\langle\omega_\theta\rangle R/U_\infty$ and (*b*) shows the mean pressure coefficient $\langle C_p\rangle$.

As discussed previously, the open rotor has a much lower pressure than the ducted rotor at the same thrust ($J=1.11$) even though the loading, and thus circulation shed, at the blade tip is larger for the ducted $J=1.11$ case. This apparent conflict can be explained by the chordwise distribution of suction at the blade tip seen in 13. Since the blade suction forms across the entire chordwise length of the tip in the ducted rotor $J=1.11$ case, the leakage

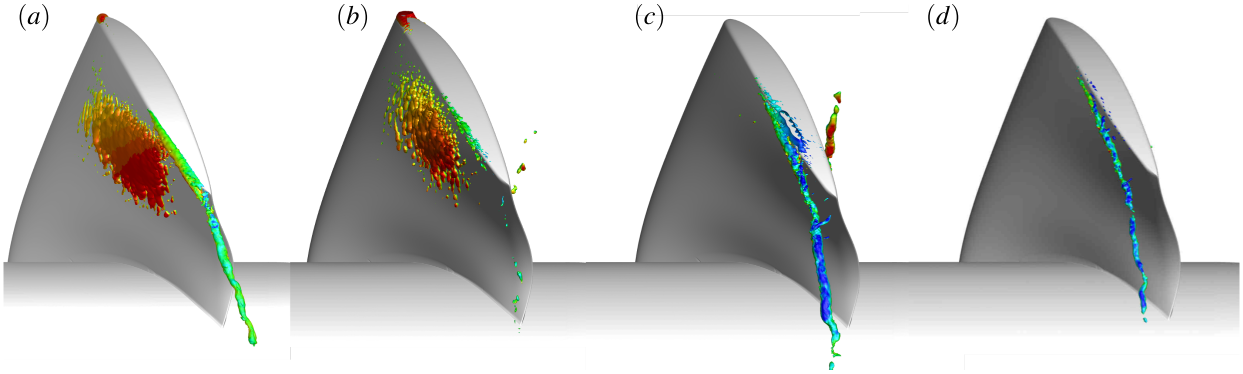

Figure 15: Instantaneous pressure isosurfaces across the range of advance ratios colored by axial velocity. (*a*) $C_p = -2.0$ for $J = 0.98$ open, (*b*) $C_p = -2.0$ for $J = 1.11$ ducted, (*c*) $C_p = -3.5$ for $J = 0.98$ ducted, (*d*) $C_p = -7.0$ for $J = 0.87$ ducted.

flow develops nearer to the leading edge which forces the primary vortex to separate upstream from the trailing edge. At the trailing edge, the shed circulation from the lift at the blade tip is therefore spread out into two distinct regions of positive ω_θ. This split in the shed circulation results in the increased pressure of the tip vortex core for the ducted case.

This section has examined tip vortex flow for a range of rotor operating conditions. The LES results find agreement with the observations made in Oweis et al. (2006a) that the open rotor has a stronger tip leakage vortex than the ducted rotor. This difference is explained by the open rotor having a strong pressure differential across the tip concentrated near the blade trailing edge, while the ducted rotor at the same thrust has a more consistent lower tip pressure differential along the chord. This results in the open rotor developing a tip leakage flow further upstream in the chordwise direction, resulting in a separated leakage vortex which is offset at the blade trailing edge. Meanwhile, decreasing the advance ratio on the ducted rotor is seen to move the primary leakage vortex separation point further upstream in the chordwise direction, increase the offset distance at the trailing edge, increase the circulation, and reduce the leakage vortex core pressure. Finally, secondary structures of low pressure are seen to wrap helically around the primary leakage vortex core at both $J = 0.98$ and $J = 0.87$ for the ducted rotor. The interaction of these primary and secondary vortices is most important to inception at the design condition $J = 0.98$. The nature of instantaneous vortex structures is examined in more depth in the next section.

Instantaneous Flow Field

This section examines the instantaneous LES results on the fine mesh for the ducted rotor at $J = 0.98$ to provide a more in-depth analysis of flow structures and their relation to cavitation inception. Assessment of the instantaneous flow field reveals the primary leakage vortex has a clearly identifiable region of low pressure, visualized with an isosurface of $C_p = -3.9$ in Figure 16(a). No coherent trailing edge vortex is visible in the pressure field. However, side lobes of low pressure are seen wrapping helically around the primary vortex core, evidence of vortex mergers occurring both upstream and downstream of the blade trailing edge. Side lobes are seen to correspond to areas of high voritcity magnitude. An isosurface of $C_p = -4.7$ (transparent gray) along with isosurfaces of Q-criterion are shown in Figure 16(*b*), (*c*), and (*d*) revealing a more complex flow field of small-scale vortex structures. The Q-criterion is the second invariant of the velocity gradient tensor (Hunt et al., 1988), defined as

$$Q = \frac{1}{2}|\omega| - S_{ij}S_{ij} = \frac{\partial u_i}{\partial x_j}\frac{\partial u_j}{\partial x_i} \tag{7}$$

where S_{ij} is the velocity strain rate tensor and ω is the vorticity vector. For incompressible flows, it can also be shown that

$$Q = \frac{1}{2\rho}\nabla^2 p \tag{8}$$

demonstrating that Q behaves as a source term for pressure (Dubief and Delcayre, 2000). In Figure 16(b), isosurfaces of $Q = 100800 s^{-2}$ are colored by the local pressure coefficient C_p. The trailing edge wake is seen to remain at a pressure higher than ambient (P_∞) and much higher than the pressure in the primary vortex core. This is evidence that, instantaneously, there are no coherent vortex structures at the trailing edge with strong enough rotation to induce a distinct low-pressure core. In Figure 16(*c*) and (*d*) a higher value of $Q = 172800 s^{-2}$ is visualized to highlight only the strongest

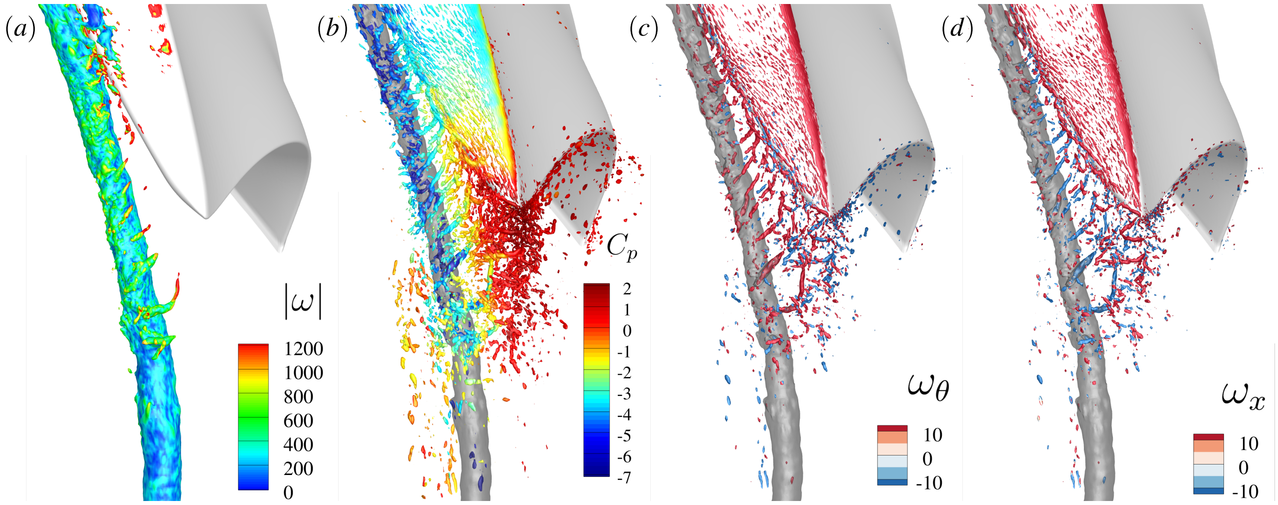

Figure 16: (*a*) Instantaneous iso-contours of the pressure coefficient $C_p = -3.9$ coloured by the vorticity magnitude $|\omega|$. (*b*) Instantaneous iso-contours of $QR^2/U_\infty^2 = 100800$ coloured by the pressure coefficient C_p. Instantaneous iso-contours of $QR^2/U_\infty^2 = 172800$ coloured by the azimuthal vorticity ω_θ in (*c*), and coloured by axial vorticity ω_x in (*d*). An isosurface of $C_p = -4.7$ is also displayed in transparent gray in $(b-c)$.

vortex structures. In Figure 16(c), isosurfaces of Q are colored by the sign of the azimuthal vorticity ω_θ, revealing that the flow separating off the trailing edge is a mixture of small-scale vortices co-rotating (red) and counter-rotating (blue) with the primary leakage vortex. These observations of the instantaneous LES results counter the description of the mean flow field given by Chesnakas and Jessup (2003) and shed additional insights on the descriptions of the instantaneous flow field given by Oweis et al. (2006b).

Vortices generated in the blade tip boundary layer are seen in Figure 16(*c*) and (*d*) to be oriented perpendicular to the leakage flow. There is also significant fine-scale vorticity throughout the separation sheet connecting the blade tip to the primary leakage vortex core aft of the core separation point. Interestingly, the separation sheet is seen to have instantaneous vortex structures that are aligned nearly parallel to the leakage flow - with a positive u_θ and negative u_x. This observation indicates that the separation sheet is not simply transporting vorticity from the blade tip boundary layer. Rather, the shear of the separation sheet itself is dynamically relevant to the vorticity being fed to the primary leakage vortex core, which is discussed further in the next section (titled “Mean Flow Field”). The orientation and placement of those leakage flow-aligned vortices in the separation sheet correspond to the previously discussed side lobes of low-pressure wrapping helically around the primary vortex core. A majority of the vortices in the separation sheet upstream from the blade tip trailing edge rotate in the positive θ direction, co-rotating with the primary leakage vortex, while the small scale vortices from the trailing edge wake are more likely to counter-rotate with the primary vortex. Likewise, a majority of the vortices in the separation sheet upstream from the blade tip trailing edge have positve ω_x, while the small scale vortices from the trailing edge wake are more likely to have negative ω_x. Merger of these small-scale vortices with the primary leakage vortex occurs all along the separated primary core's length to more than 30% of the chord length downstream from the trailing edge. The location of the lowest mean pressure is seen to occur 15% of the chord length downstream of the blade tip, which coincides with an area of strong interaction between the trailing edge wake and the primary leakage vortex.

There is also an additional counter-rotating vortex visible to the left of the primary leakage vortex in Figure 16($b-d$). This counter-rotating vortex is located upstream in the axial direction and above the primary leakage vortex core in the radial direction and oriented nearly parallel to the primary vortex core. This upstream vortex results from the rollup of the duct boundary layer vorticity that occurs as the reversed leakage flow ($u_x < 0$) meets the turbulent inflow ($u_x > 0$). Upstream counter-rotating vortices are seen to move downward in the radial direction and interact with the primary leakage vortex structures between 20% and 50% of the chord length downstream of the blade tip. The overall picture of vortex interactions in the wake of a ducted propulsor suggested by LES consists of co- and counter-rotating small-scale vortices from the leakage flow, separation sheet, trailing edge wake, and induced upstream vortex. Cavitation inception was observed experimentally at around 50% chord length downstream of the blade tip.

The complex and unsteady interactions of these diverse small-scale vortices could explain this observation.

A schematic illustration of the significant vortex flow structures suggested by the current LES is presented in Figure 17. The blade is viewed from above the tip looking down at the trailing edge such that the blade rotates upward in the plane of the page. The primary leakage vortex is illustrated in pink and detaches from the blade upstream from the trailing edge (A). Aft of the primary vortex separation, additional vorticity of the blade tip boundary layer is shed and forms a separation sheet (B). The separation sheet is composed of vortices both perpendicular to the leakage flow (blue) and parallel to the leakage flow (green). At the trailing edge, additional vorticity is shed from the blade pressure side boundary layer (C). After the blade passes, the vortex structures of the separation sheet and boundary layer move above the primary leakage vortex (D). The interaction of the reversed leakage flow with the incoming duct boundary layer induces a counter-rotating vortex parallel to the primary vortex and upstream in the axial direction, which is shown in yellow (E). The trailing edge vortex observed by Chesnakas and Jessup (2003) at higher Re_{tip} (Figure 4(a)) was not seen in the present LES results and is therefore omitted from Figure 17.

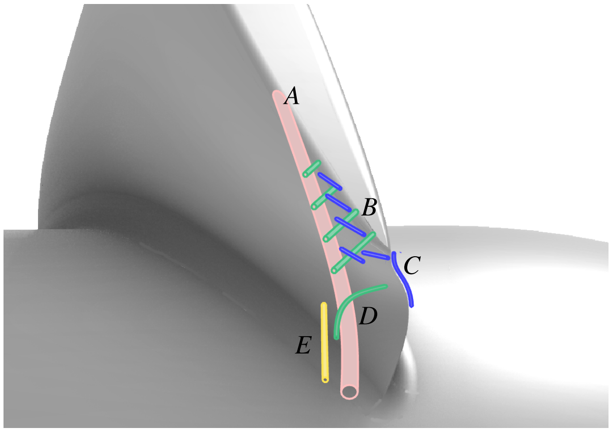

Figure 17: Schematic of significant vortex structures in the ducted propeller flow near peak efficiency. Pink represents the primary leakage vortex. Blue represents vortices originating in the blade boundary layer. Green represents the leakage-flow aligned vortices of the separation sheet. Yellow is the induced counter-rotating vortex.

To estimate the probable location of cavitation inception, locations of extreme low-pressure events are collected for the fine grid over 4 propeller revolutions. The joint probability density function (PDF) in $x-\theta$ space is shown in Figure 18 for (a) $C_p < -5.6$ and (b) $C_p < -6.6$. The joint PDF is defined discretely by binning low pressure events into discrete regions of $x-\theta$ space and dividing the number of samples in each bin by the total number of samples and the bin area. Note that these threshold values of C_p are not the lowest that occur during the simulation. Lower pressure events are increasingly rare and, as a result, would require additional run time to capture enough events such that probability distributions are converged. The joint PDF of $C_p < -5.6$ in Figure 18(a) shows a clear bimodal distribution, with low-pressure events likely to occur both upstream of the trailing edge in the primary vortex core and the blade wake region of vortex mergers described earlier. Meanwhile, 18(b) shows that even lower pressure events of $C_p < -6.6$ are strongly concentrated in the vortex merger region in the blade wake, specifically at $s = 0.12$ and $x/r = 0.18$.

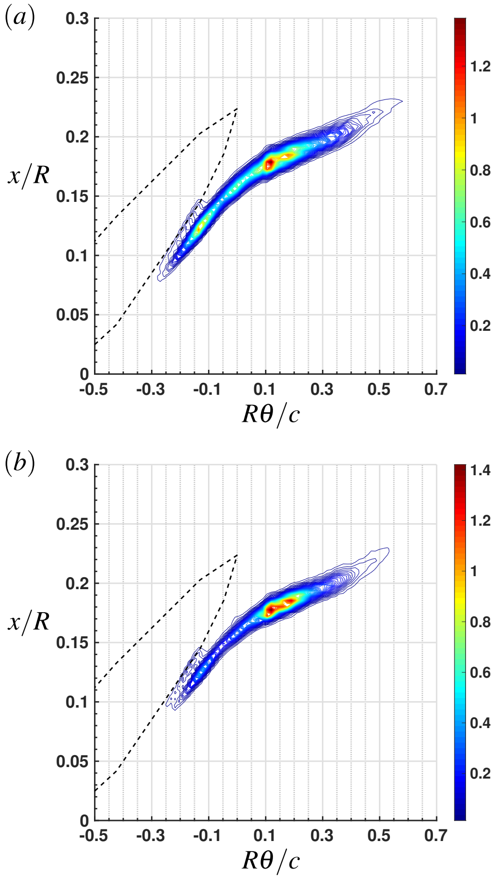

Figure 18: The joint PDF of low pressure events in $x-\theta$ space for the fine grid for (a) $C_p < -5.6$ and (b) $C_p < -6.6$. The dashed line is the blade outline.

This section has provided a more complex picture of the instantaneous tip vortex flow field than that provided by Chesnakas and Jessup (2003) and Oweis et al. (2006b). A coherent vortex emanating from the trailing edge is not seen in the LES results. Instantaneous vortex structures aligned with the tip leakage flow were observed throughout the separation sheet connecting the separated primary vortex core to the blade tip boundary layer. These leakage flow-aligned structures are observed both forward and aft of the blade trailing edge and found to correlate with side lobes of low pressure wrapping around the primary vortex core. This suggests that the trailing edge vortex discussed by Chesnakas and Jessup (2003) and Oweis et al. (2006b) is not generated by the blade trailing edge itself but within the separation sheet. Despite offering a somewhat different description of the relevant mechanisms driving the flow, the current LES results find agreement with the experimental observation that secondary vortex structures near the blade trailing edge were likely to cavitate during the merger process with the primary vortex, as evidenced by the statistics of low pressure events provided in Figure 18(*b*).

Mean Flow Field

This section examines the time-averaged flow field of the LES results on the fine mesh at $J = 0.98$ to provide a more in-depth explanation of the formation of instantaneous flow structures observed in the previous section.

Figure 19(a) shows slices through the mean flow field colored by the azimuthal vorticity. While no coherent tailing edge vortex is visible in the instantaneous flow, the time-averaged flow does reveal a distinct vortex emanating from the blade trailing edge as well as the induced upstream counter-rotating vortex. The primary vortex core is visible as a region of strong positive vorticity which originates near the mid-chord at the blade suction side tip. The primary vortex core is seen to separate aft of the mid-chord but upstream of the trailing edge and is offset in the axial direction. The separation sheet connecting the separated primary vortex core is visible as another region of strong positive azimuthal vorticity. Aft of the trailing edge, the separation sheet rolls up into a second coherent vortex co-rotating with the primary leakage vortex. The pressure side blade wake is visible as a sheet of strong counter-rotating vorticity. The upstream-induced vortex is also visible as a region of strong counter-rotating vorticity located above the primary vortex core in the radial direction. The induced vortex originates from the rollup of the tip leakage flow duct boundary layer after the blade passes by. The rollup can be explained by the removal of the strong adverse pressure gradient created by the blade's passage which generates the reversed leakage flow in the tip gap.

Figure 19(b) shows slices colored by the mean pressure coefficient. A strong pressure gradient across the tip gap can be seen, which is driving the leakage flow. The location of the primary vortex core seen in 19(a) coincides with a strong low pressure, as expected. Outside the tip vortex, the suction side region of the blade is below P_∞ forward of the trailing edge ($s < 0$) but above P_∞ aft of the trailing edge ($s > 0$). This is relevant for cavitation prediction in the sense that an idealized vortex model links vortex circulation to the pressure differential between the core and local ambient pressure. For the core to be at vapor pressure, the circulation of an idealized vortex would need to be larger aft of the trailing edge than it would upstream nearer to the blade suction peak. The LES results show that vorticity is constantly being fed into the primary vortex from the blade tip boundary layer and separation sheet, which causes the primary vortex to strengthen in circulation as s increases. This tradeoff between the increasing ambient pressure and increasing circulation with increasing s could potentially help explain the bimodal nature of the instantaneous pressure PDF seen in Figure 18(a).

Figure 19(c) displays the mean-square pressure fluctuation, which is a useful measurement of the unsteadiness of the vortex structures seen in the mean flow field in Figure 19(a). Regions of high $\langle p'p' \rangle$ are visible in the tip trailing edge region, the primary separation sheet, and on either side in the axial direction of the primary vortex core downstream. This indicates that the mean vortices observed in these regions have significant wandering of the core location. This is consistent with the interactions of small-scale vortex structures discussed earlier. More specifically, the observation of high mean-square pressure in the tip trailing edge provides evidence that the observed coherent trailing edge vortex observed in the experiments of Chesnakas and Jessup (2003) and Oweis et al. (2006b) is specifically a mean-flow phenomenon and that secondary vortices observed to cavitate during interaction with the primary leakage vortex may originate anywhere in the separation sheet connecting the blade tip boundary layer to the primary core.

Figure 19(d) shows that the area between the induced upstream vortex and the edge of the primary leakage vortex is associated with a region of high turbulent fluctuation in the axial flow, $\langle u_x'u_x' \rangle$. This indicates that this vortex is closely associated with the interaction of the tip leakage flow in the $-x$-direction and the incoming turbulent duct boundary layer in the $+x$-direction. A similar observation was made in the axial waterjet experiments of Wu et al. (2012). This conclusion suggests that simulations performed with a steady or laminar inflow to the propulsor could predict a different vortex structure in the blade wake. Additionally, this suggests that the thickness of the duct boundary layer relative to the tip gap spacing could be an important scaling parameter that is non-trivial to achieve when comparing across experimental facilities.

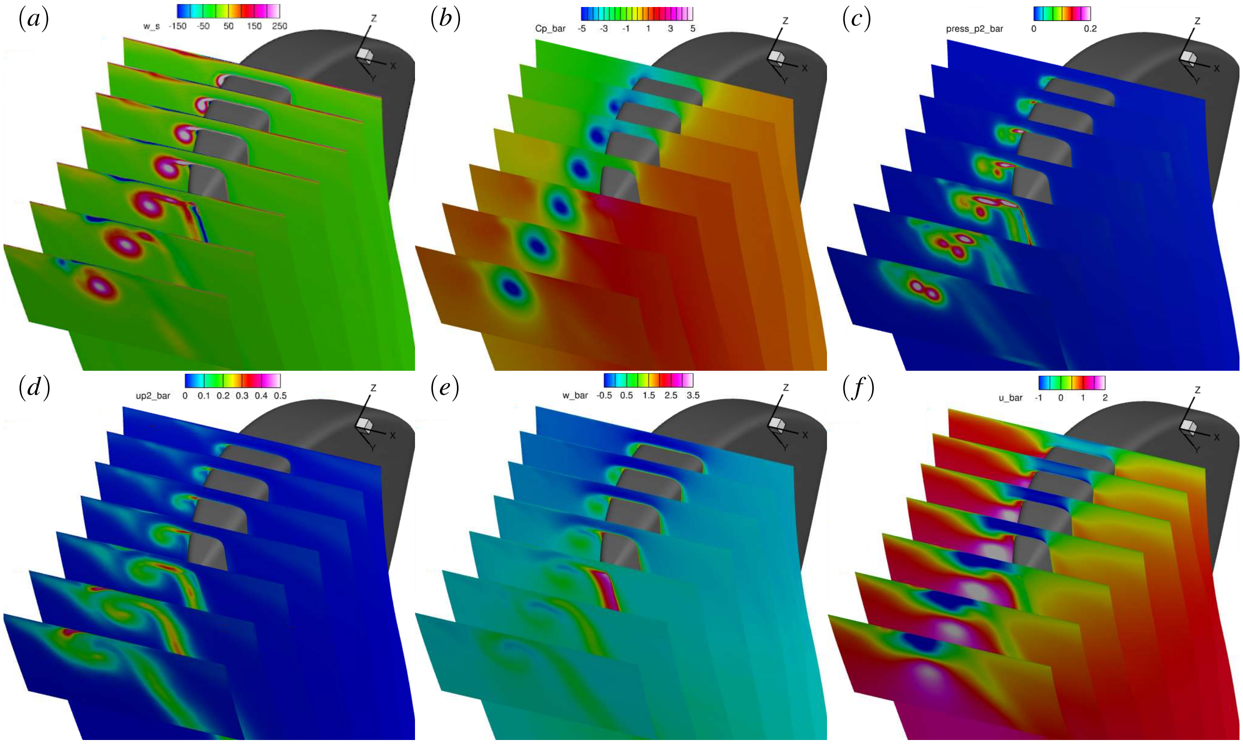

Figure 19: Slices through the time-averaged LES flow field computed on the fine grid at $J = 0.98$ colored by (*a*) Azimuthal vorticity $\langle \omega_\theta \rangle$, (*b*) Pressure coefficient $\langle C_P \rangle$, (*c*) Mean-square pressure fluctuation $\langle p'p' \rangle$, (*d*) Mean-square axial velocity fluctuation $\langle u'_x u'_x \rangle$, (*e*) Azimuthal velocity $\langle u_\theta \rangle$, and (*f*) Axial velocity $\langle u_x \rangle$. The flow field quantities are normalized appropriately using ρ, U_∞ and R.

The mean flow also provides insight into the production of vortices aligned with the leakage flow, which were observed to wrap helically around the primary vortex in the preceding section. Figure 19 shows the contours of the mean azimuthal velocity (e) and axial velocity (f) in the inertial frame. In addition to the primary shear in the axial flow (dU_x/dr), there is also a secondary shear the in the azimuthal flow (dU_θ/dr), representing a skewed shear layer. Skewed shear layers are a well-studied phenomenon and are known to produce vorticity aligned with the local flow (Lu and Lele, 1993; Fiedler et al., 1998; Saric et al., 2003; Wernz et al., 2006; Meldi et al., 2020). Additionally, skewed shear layers have an instability associated with the inflection point of the velocity profile. Profiles of mean flow components across the separation sheet are shown in Figure 21. Profiles are extracted in the radial direction at 3 locations upstream from the trailing edge $s = -0.018, -0.065, -0.111$ and located halfway between the blade suction side and the primary vortex core in the x-direction. The vertical axis shows the radial coordinate normalized by the tip gap size h and centered on the blade tip at $r = R$. Above the separation sheet in the tip leakage flow, the axial velocity is strongly negative and the azimuthal velocity is moderately negative (moving opposite to the blade). The azimuthal velocity is strongly positive (moving with the blade) just at the blade tip $r/R = 1$ which is a result of the fact that fluid at this location originates in the blade boundary layer before separating off the suction side blade tip. Below the separation sheet, the azimuthal velocity is moderately positive (again moving with the blade) while the axial velocity is strongly positive as a result of the radial circulation (or lift) produced by the blade passage. The relative strength of the flow components changes significantly with s in the tip leakage flow, with profiles closer to the trailing edge having weaker azimuthal vorticity and stronger axial velocity. Below the separation sheet, the dependence on s is weaker. The axial velocity profile has a single inflection point at $r/R = 0.998$ while the azimuthal velocity profile has two inflection points at $r/R = 1.002$ and 0.995, respectively.

The impact of the skew of the shear layer on turbulent structures is clearly visible in the Reynolds stress tensor components displayed in Figure 20. 20(a) displays slices of $\langle u'_x u'_r \rangle$ which demonstrates that in the separation sheet, the axial and radial velocity fluctuations are positively correlated. Meanwhile, 20(b) shows that the radial and azimuthal velocity fluctuations $\langle u'_r u'_\theta \rangle$ are also positively correlated. Together, this provides

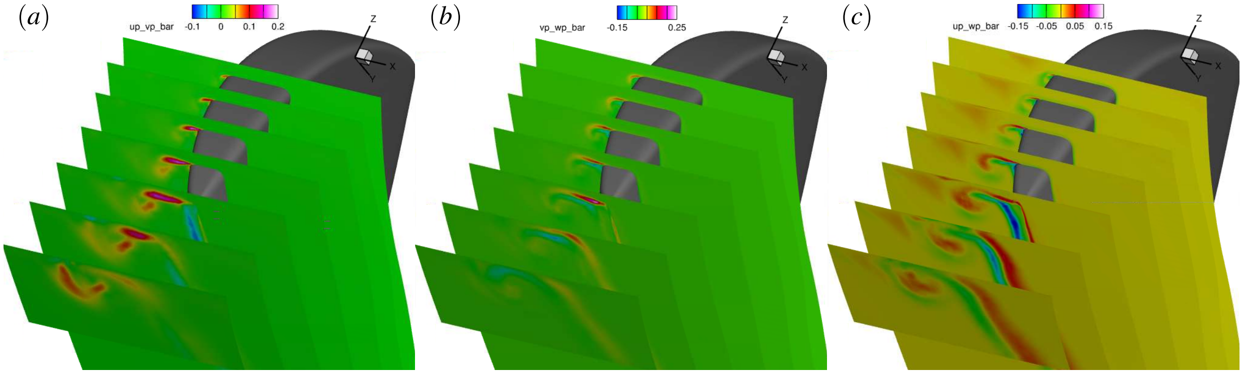

Figure 20: Reynolds stress tensor off-diagonal components from the fine grid LES at $J = 0.98$ colored by (a) $\langle u'_x u'_r \rangle$, ($b$) $\langle u'_r u'_\theta \rangle$, ($c$) $\langle u'_x u'_\theta \rangle$. The flow field quantities are normalized appropriately using ρ, U_∞ and R.

evidence of instantaneous vortices that are co-rotating with the primary vortex but with a vortex core somewhat aligned with the axial direction. Figure 20(c) shows that correlation of $\langle u'_x u'_\theta \rangle$ flips sign on either side of the separation sheet. Above the separation sheet in the radial direction, fluctuations are positively correlated, while below the separation sheet, they are negatively correlated. However, correlations of $\langle u'_x u'_\theta \rangle$ are approximately 4 times smaller than correlations of either $\langle u'_x u'_r \rangle$ or $\langle u'_r u'_\theta \rangle$ indicating that instantaneous vortices are unlikely to have a core aligned with the radial direction. This is the expected result given that the mean shear is much larger in the radial direction.

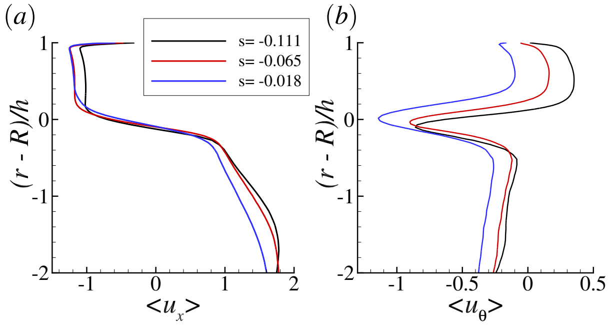

Figure 21: Mean velocity profiles across the separation sheet connecting the primary vortex core to blade tip boundary layer (a) Axial velocity $\langle U_x \rangle / U_\infty$ and (b) Azimuthal velocity $\langle U_\theta \rangle / U_\infty$.

In this section, mean flow features driving tip vortex structures for a ducted rotor at $J = 0.98$ have been examined. The coherent trailing edge vortex described by Chesnakas and Jessup (2003) were seen in the LES results to be a feature of large-time averages. Meanwhile, instability mechanisms not previously identified in the ducted propulsor flow were observed in the separation sheet connecting the blade tip boundary layer to the separated leakage vortex core. The importance of these instability mechanisms to the vortex structures of the separation sheet discussed in the "Instantaneous Flow Field" section was shown in the off-diagonal terms of the Reynolds shear stress.

Conclusion

Unstructured overset Large Eddy Simulations (LES) are used to study the propeller P5407 at multiple advance ratios and in both ducted and open configurations. The overset method enables the creation of fully hexahedral grids with high resolution that represents the complex geometries of the rotor blades and duct. The sensitivity of the propeller thrust K_T to the inflow was observed and quantified near $J = 1.11$. At design advance ratio $J = 0.98$, LES predicts the propeller loads within the experimental scatter when matching the incoming mass flow rate. The time-averaged flow field is compared to experimental Laser Doppler Velocimetry (LDV), showing agreement in the mean tip vortex strength and position.

Assessing the pressure field reveals a strong leakage vortex that separates upstream from the trailing edge in the ducted rotor, as observed in the experiments. On the other hand, no persistent vortex is found to emanate from the trailing edge. Rather, the tip leakage flow is found to instantaneously be composed of a complex mixture of small-scale vortices. The leakage flow generates rolling vortices in the blade boundary layer oriented perpendicular to the leakage flow. The leakage flow then separates off the suction side blade tip resulting in the rollup of the leakage flow in the primary leakage vortex. Aft of the primary vortex separation point, a separation sheet connects the primary core to the blade tip boundary layer. The separation sheet is shown to resemble a skewed mixing layer with two inflection points in the velocity profiles representing a source of instability in the flow not previously identified in the literature. The separation sheet is seen to contain instantaneous vortices aligned with the leakage flow. A majority, but not all, of these small-scale vortices in the separation sheet co-rotate with the primary core representing a source of additional circulation of the primary vortex after the separation point. The orbit and merger of vortices from the separation sheet into the primary vortex core is seen to induce side-lobes of low pressure wrapping helically around the primary vortex core both forward and aft of the trailing edge. The trailing edge wake is found to contain a larger concentration of counter-rotating vortices than the separation sheet upstream of the trailing edge. Additional counter-rotating vortices not previously observed in literature for P5407 are observed upstream and tied to the interaction of the tip leakage flow with the turbulent inflow duct boundary layer. Statistics of the instantaneous low-pressure events show a higher likelihood of cavitation inception between 10% and 15% of the tip chord length downstream from the trailing edge.

The vortex structure of the ducted rotor was also examined across a range of advance ratios corresponding to $\pm 14\%$ of design J. The primary leakage vortex is seen to separate further towards the leading edge at lower advance ratios and closer towards the trailing edge at higher advance ratios. As a result, at a given azimuthal location relative to the trailing edge, the primary vortex core and pressure minimum move upstream as the advance ratio decreases. At high advance ratios, global instantaneous pressure minima are seen to occur outside the vortex core on the blade surface. These pressure minima are tied to the flow acceleration around regions of high curvature. Meanwhile, the bulk pressure in the tip gap is seen to reduce at lower J. As such, the interactions between primary and secondary vortices are most important to inception near design J.

Comparisons between the ducted and the open rotor at the same thrust reveal that the open rotor has a stronger tip vortex with a lower core pressure. This occurs even though the open rotor has less loading near the tip. The observation is explained by the fact that the circulation shed at the tip of the ducted rotor is split among two separate vortex cores. The presence of the duct is also seen to alter the local angle of attack experienced by blade sections near the tip when comparing the ducted to the open rotor at the same advance ratio.

Acknowledgements

This work was supported by the United States Office of Naval Research (ONR) under ONR Grant N00014-18-1-2356 with Dr. Ki-Han Kim and Dr. Yin Lu Young as grant monitors. This work was also supported by the Naval Surface Warfare Center In-house Laboratory Independent Research (ILIR) program under program managers Dr. Jack Price and Dr. Krista Lossing. Computational resources were provided by the Department of Defense (DoD) High Performance Computing Modernization Program (HPCMP). Simulations were performed on the HPE Cray EX system Narwhal at the Naval Oceanographic Office (NAVO) at Stennis Space Center, Mississippi, and the HPE Cray EX system Warhawk at the Air Force Research Laboratory (AFRL) at Wright Patterson Air Force Base, Ohio.

References

Brewer, Wesley Huntington. On simulating tip-leakage vortex flow to study the nature of cavitation inception. Mississippi State University, 2002.

Chesnakas, Christopher J and Jessup, Stuart D. “Tip-vortex induced cavitation on a ducted propulsor”. In Fluids Engineering Division Summer Meeting, volume 36967, pages 257–267, 2003.

Dubief, Yves and Delcayre, Franck. “On coherent-vortex identification in turbulence”. Journal of Turbulence, 1: N11, 2000. doi: 10.1088/1468-5248/1/1/011.

Fiedler, H.E, Nayeri, C, Spieweg, R, and Paschereit, C.O. “Three-dimensional mixing layers and their relatives”. Experimental Thermal and Fluid Science, 16(1):3–21, 1998. ISSN 0894-1777. doi: https://doi.org/10.1016/S0894-1777(97)10003-6.

Germano, M., Piomelli, U., Moin, P., and Cabot, W. H. “A dynamic subgrid–scale eddy viscosity model”. Physics of Fluids A, 3:7:1760, 1991.

Horne, W. J. and Mahesh, K. “A massively-parallel unstructured overset method for mesh connectivity”. Journal of Computational Physics, 376:585–596, 2019a.

Horne, W. J. and Mahesh, K. “A massively-parallel unstructured overset method to simulate moving bodies in turbulent flows”. Journal of Computational Physics, 397:108–790, 2019b.

Horne, Wyatt James and Mahesh, Krishnan. “A hardware accelerated unstructured overset method to simulate turbulent fluid flow”. Journal of Computational Physics, 444, 2021.

Hsiao, C-T and Chahine, GL. “Numerical study of cavitation inception due to vortex/vortex interaction in a ducted propulsor”. Journal of Ship Research, 52(02): 114–123, 2008.

Hsiao, CT and Chahine, GL. “Effect of unsteady turbulent fluctuations on vortex/vortex/nuclei interactions”. In 26th Naval Hydrodynamics Symposium, Rome, Italy, 2006.

Hunt, J. C. R., Wray, A. A., and Moin, P. “Eddies, streams, and convergence zones in turbulent flows”. Center for Turbulence Research Report CTR-S88, page 193, 1988.

Judge, Carolyn Q, Oweis, Ghanem F, Ceccio, Steven L, Jessup, Stuart D, Chesnakas, Christopher J, and Fry, David J. “Tip-leakage vortex inception on a ducted rotor”. In CAV 2001: Fourth International Symposium on Cavitation. University of Michigan, 2001.

Kawakita, Chiharu. “A surface panel method for ducted propellers with new wake model based on velocity measurements”. Journal of the Society of Naval Architects of Japan, 1992(172):187–202, 1992. doi: 10.2534/jjasnaoe1968.1992.172_187.

Kim, Jin, Paterson, Eric G, and Stern, Frederick. “Rans simulation of ducted marine propulsor flow including subvisual cavitation and acoustic modeling”. Journal of Fluids Engineering, 128:799–810, 2006.

Kroll, T. Large-eddy simulation of marine propeller flows using an unstructured overset method. PhD thesis, University of Minnesota, 2022.

Lilly, D. K. “A proposed modification of the Germano subgrid–scale closure model”. Physics of Fluids A, 4:3: 633, 1992.

Lu, Ganyu and Lele, Sanjiva K. “Inviscid instability of a skewed compressible mixing layer”. Journal of Fluid Mechanics, 249:441–463, 1993. doi: 10.1017/S0022112093001247.

Mahesh, K., Constantinescu, G., and Moin, P. “A numerical method for large–eddy simulation in complex geometries”. Journal of Computational Physics, 197:1:215, 2004.

Meldi, M., Mariotti, A., Salvetti, M. V., and Sagaut, P. “Numerical investigation of skewed spatially evolving mixing layers”. Journal of Fluid Mechanics, 897:A35, 2020. doi: 10.1017/jfm.2020.407.

Miorini, Rinaldo L, Wu, Huixuan, and Katz, Joseph. “The internal structure of the tip leakage vortex within the rotor of an axial waterjet pump”. Journal of Turbomachinery, 50(11):2574–2587, 2012.

Oweis, G, Fry, D., Chesnakas, C., Jessup, S., and Ceccio, S. “Tip-leakage flow part 2 comparison between the ducted and un-ducted rotor”. Journal of Fluids Engineering, 128:765–773, 2006a.

Oweis, G. F. An Experimental Investigation into the Dynamics of Propeller Tip Vortices and the Associated Cavitation Noise. PhD thesis, University of Michigan, USA, 2003.

Oweis, G. F., Fry, D., Chesnakas, C., Jessup, S., and Ceccio, S. L. “Development of a tip-leakage flow part 1 the flow over a range of reynolds numbers”. Journal of Fluids Engineering, 128:751–764, 2006b.

Park, N. and Mahesh, K. “Reduction of the Germano-identity error in the dynamic Smagorinsky model”. Physics of Fluids (1994-present), 21(6): 065106, 2009.

Saric, William S., Reed, Helen L., and White, Edward B. “Stability and transition of three-dimensional boundary layers”. Annual Review of Fluid Mechanics, 35(1): 413–440, 2003. doi: 10.1146/annurev.fluid.35.101101.161045.

van Manen, J.D. “Effect of radial load distribution on the performance of shrouded propellers1”, 1962.

Verma, A. and Mahesh, K. “A Lagrangian subgrid-scale model with dynamic estimation of Lagrangian time scale for large eddy simulation of complex flows”. Physics of Fluids (1994-present), 24(8):085101, 2012.

Wernz, Stefan, Ringwald, Heike, and Fasel, Hermann. “Numerical investigation of instabilities in three-dimensional skewed shear layers”. In 3rd AIAA Flow Control Conference, 2006. doi: 10.2514/6.2006-3347.

Wu, Huixuan, Tan, David, Miorini, Rinaldo L, and Katz, Joseph. “Three-dimensional flow structures and associated turbulence in the tip region of a waterjet pump rotor blade”. Experiments in fluids, 51(6): 1721–1737, 2011.

Wu, Huixuan, Miorini, Rinaldo L, Tan, David, and Katz, Joseph. “Turbulence within the tip-leakage vortex of an axial waterjet pump”. AIAA journal, 134, 2012.

Discussion 1

Moustafa Abdel-Maksoud
Institute for Fluid Dynamics and Ship Theory
Hamburg University of Technology (TUHH)

In the paper, the results of a comprehensive LES-study on the tip vortex flow of a ducted propulsor geometry are presented. The validation is carried out using experimental data published by Chesnakas and Jessup as well as by Oweis. The focus is given to cavitation inception and the unsteady interactions between multiple vortices in the tip region. The agreement between the LES- and LDV-results is very high. The simulation results show the instantaneous pressure distribution on the rotor blades and the vortical structure of the separated leakage flow, which rolls up into a coherent leakage vortex.

In addition to investigating of the tip leakage flow in a ducted propulsor, the flow on an open rotor is studied and the properties of the tip vortex flows at the same thrust loading condition as well as at different loading conditions of the ducted propulsor are compared. These results are very valuable as very limited numerical and experimental data is available regarding the influence of the duct on the tip vortex flow structure on the rotor blades. In order to be able to analyze the information presented in Figure 14, it is important to include the evolution of the vorticity and core radius in the figure, as well as the pressure along the vortex centre, which can be estimated based on the maximum Q value or the minimum pressure. In addition, it can be very helpful to evaluate the leakage flow rate as a function of the pressure difference between the suction blade sides for the different thrust loading conditions of the ducted propulsor and at different distances from the tip of the open water rotor.

Finally, I would like to thank the authors for their valuable contribution! Congratulations on the high quality of the study presented in the paper and the detailed discussion of the results.

Responses to Discussion Comments

The discusser is thanked for their valuable suggestions. Future analysis of the advance ratio effect can incorporate the suggested plots of leakage vortex maximum Q as a function of distance along the vortex core after separation. The leakage mass flow rate velocities could also be quantified.

Discussion 2

Jin-Keun Choi
Naval Surface Warfare Center - Carderock Division
Naval Architecture and Engineering Department (872)

Authors' work on the ducted propeller tip flow using large eddy simulation (LES) approach is a welcome addition to the community's long effort to tackle the problem of P5407/P5206 tip vortex. Congratulations to the author for revealing the new details of the tip flow using computationally intensive LES approach!

In spite of these new findings, the LES approach in this paper was not able to capture the tip trailing edge vortex that was persistent in experiments as shown in Figure 4 of the paper. Reynolds Averaged Navier-Stokes equation solvers and Detached Eddy Simulations (DES) were able to capture this trailing edge vortex. Do authors have any insight on why the LES approach predicts only the small-scale eddies shedding from the trailing edge which do not form into a coherent trailing edge vortex?

One can suspect grid resolution and inflow. Could authors provide their understanding on these aspects?

- Grid resolution: Figure 5 may indicate that even the fine grid doesn't seem to fully resolve the tip trailing edge region perhaps due to the tiny scale eddies generated by the pointy tip of the trailing edge.

- Inflow: Did the uniform inflow with the numerical tripping using 0.06% inflow velocity produce correct mean velocity profile (duct boundary layer) in front of the rotor tip? The predicted velocity profile may be compared with existing LDV measurements in front of the rotor. Good agreement in the predicted mean forces may not guarantee the correctness of local inflow at the tip, which could be a relatively small contributor to the total force.

In addition, if the authors observed the roll-up of trailing vortices from inner radii trailing edge into the tip vortex, could the authors describe how well the numerical method captures the inner radii trailing vortices and their roll-up into the tip trailing edge vortex? An aspect that was not addressed much in the paper is the minimum pressure downstream in the tip vortex. It would benefit the community if the authors can discuss what LES approach offers in terms of predicting the minimum pressure in the tip vortex.

Once again, the authors' contribution to the tip vortex problem using LES is very much appreciated, and continued success in this endeavor would bring us better understanding of this complex flow.

Responses to Discussion Comments

The discusser is thanked for their thoughtful comments. The LES results do show a coherent trailing edge vortex in the mean solution. The figure below shows isosurfaces of the mean Q-criterion colored by the mean pressure coefficient. The trailing edge vortex is clearly visible but remains at a pressure above P_∞ until it wraps around the top of the primary leakage vortex. The upstream induced vortex is visible on the left of the primary leakage vortex. The Q isosurfaces below $r/R = 0.975$ are blanked for clarity.

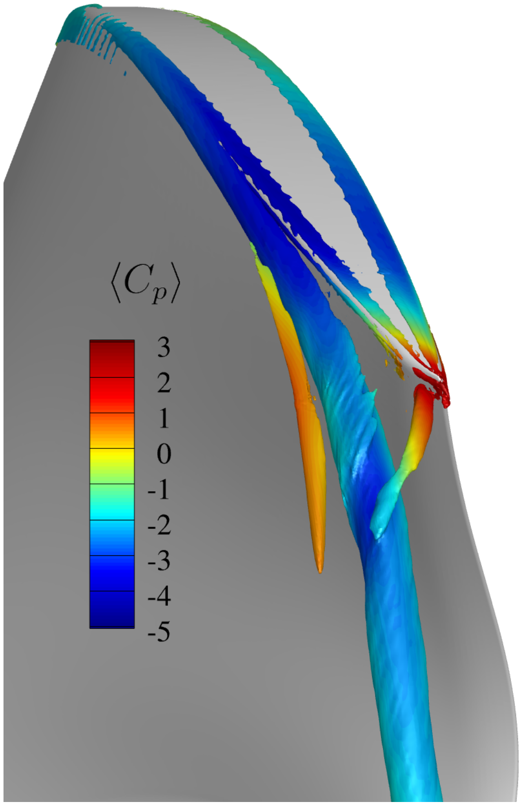

Simulations with additional grid refinement in the blade tip trailing edge region have been completed since the time this manuscript was submitted. The additional resolution did not change the conclusions reported in this paper with respect to mean pressure, turbulent stresses, or other kinematic quantities. The instantaneous low pressure statistics on the finest mesh increased likelihoods of low pressures at the trailing edge and far behind the blade trailing edge relative to the coarse mesh presented here. These tip refinement results will be reported in follow on publications. The effect of spanwise variation in inflow velocity has not been examined for reasons of computational cost.